Građevinski materijali i konstrukcije
Building Materials and Structures
journal homepage: www.buildingmaterialsstructures.com
https://doi.org/10.5937/GRMK2600005M

Original scientific paper

Analysis of vertical deflection of a simply supported timber beam using VL6180X sensor signal monitoring

Ilija M. Miličić*[1], Radomir J. Folić[2], Aleksandar D. Prokić[1]

[1] *University of Novi Sad, Faculty of Civil Engineering Subotica, Kozaračka 2a, 24000 Subotica, Serbia*
[2] *University of Novi Sad, Faculty of Technical Sciences, Dr Sime Milošević 12, 21000 Novi Sad, Serbia*

Article history

Received: 24 November 2025
Received in revised form:
22 January 2026
Accepted: 05 February 2026
Available online: 16 March 2026

Keywords

analysis,
digital signal,
VL6180X laser sensor,
beam,
displacement

ABSTRACT

In this study, the vertical displacement at the midspan of a beam is monitored using a VL6180X laser distance sensor within an experimental–theoretical framework. The proposed measurement system is simple and well suited for the acquisition of both static and dynamic structural responses. The measured data are recorded as a continuous digital signal and processed in the Arduino environment. The time-domain signals are then exported to MS Excel for further analysis using the Fast Fourier Transform (FFT). The Discrete Fourier Transform (DFT) and its inverse (iDFT) are implemented in order to validate the measured response in both the time and frequency domains. The comparison between the DFT- and FFT-based analyses indicates only negligible differences in the evaluated midspan displacement for the same vertical signal.

1 Introduction

Measurement equipment and instruments play a significant role in experimental–theoretical analyses of structural systems. Various monitoring techniques have been developed, ranging from early applications of 3D laser scanners like the Cyrax HD 2500 manufactured by Leica Geosystems to more recent approaches for assessing structural stability [1], [2–4], [5], [6–10]. However, these systems exhibit certain limitations related to data acquisition speed, number of measurement points, hardware and software implementation, as well as the methods used for processing and analyzing the measured data. To overcome the existing limitations and to address the need for new approaches in structural analysis, a novel system termed *Imm_DF_system_2021* is proposed in this study. The proposed system is intended for time-dependent monitoring of beam deflection. Deflection is a key parameter for verifying the serviceability criteria of civil engineering structures. In the present research, approximately 150 tests were conducted over a one-year period. The system is suitable for long-term monitoring of point displacements on a beam. The experimental verification of the new measurement system was carried out for time intervals ranging from 1 minute to 6 hours under static loading of a timber beam.

The core components of the system consist of a VL6180X laser sensor (Fig. 1), electronic chips, and printed circuit boards supported by dedicated software. The laser sensor is based on FlightSense™ technology, which enables the registration of relative point displacements on the beam surface independently of light refraction and/or reflection effects. The system is physically connected via USB ports to an Arduino Genuino board and operated using the Arduino 1.8.19 environment. The acquired data are automatically updated in MS Excel or MATLAB 2021a [11] and processed using user-developed algorithms based on available mathematical methods for the analysis of digital deflection signals. In particular, these procedures enable the determination of the induced kinematic quantities, such as displacement, velocity, and acceleration of the observed point, under static and dynamic excitation.For displacement measurements, a laser distance sensor is employed. The emitted laser beam is designed to comply with Class 1 laser safety limits under all operating conditions, including fault conditions, in accordance with IEC 60825-1:2007. The laser output remains within technical safety limits when the configuration follows the recommendations of STMicroelectronics and the conditions specified in [6]. It is recommended to keep the laser output power at its current level and avoid using additional optics to focus the laser beam [5].

2 Configuration of the proposed measurement system

The *Imm_DF_system_2021* proposed in this study is based on the VL6180X distance sensor (Fig. 1a). Unlike conventional infrared (IR) distance sensors, which estimate displacement from the intensity of the reflected light and therefore suffer from nonlinearity, the VL6180X does not exhibit such limitations and is able to measure point displacements with higher accuracy. The measurement

* Corresponding author:
E-mail address: ilija.m.milicic@gmail.com

range of the VL6180X sensor extends from 5 mm to 100 mm, while under certain conditions displacements of up to 150 mm can also be detected. Communication with the sensor is established via the I2C (Inter-Integrated Circuit) protocol using a set of simple programming commands. Most of the instructions are executed internally by the sensor, while data transmission is performed through the Arduino library to the microcontroller Arduino ATmega2560. As shown in Fig. 1b, the sensor includes two GPIO (general-purpose input/output) pins and one SHDN (shutdown) pin that are not part of the I2C interface and are therefore not used in this study. This is related to the importance of understanding how the infrared laser beam propagates, reflects, and is absorbed by the target surface. Along the optical path to the surface, the reflected signal must remain sufficiently strong and suffer minimal losses to be relevant for accurate displacement measurement [6–7].

It has been observed that most infrared (IR) distance sensors consist of a transmitting and a receiving unit. The received radiation is detected by a photodiode, which measures the intensity of the reflected light as a function of the displacement of a point on the beam surface [6]. Since the intensity of the reflected signal depends on the surface quality and color of the beam (Fig. 2b), different levels of absorbed and reflected radiation may occur at the same distance. Therefore, the measured signal intensity is influenced by both the color (Fig. 2b) and the surface condition of the beam material. To eliminate this dependency, the distance to the target surface is determined using the Time-of-Flight (ToF) principle, i.e., by measuring the time required for a laser pulse to pass from the transmitter to the beam surface and back to the receiver. As described in [16], the ToF method employs a narrow-pulsed laser beam in combination with a time-to-digital converter (TDC) to record the time difference between the emitted and received signals. By combining the ToF principle with intensity-based IR measurements, the relative displacement of a point on the beam surface can be computed in software. In this approach, the displacement is first obtained from the ToF measurement, while the surface type and condition are subsequently assessed from the intensity of the reflected signal. By measuring the round-trip travel time of the laser pulse, the displacement can be determined independently of the amount of reflected laser radiation [8].

The directed laser beam propagates at a constant velocity in air; therefore, the distance of the reflected signal is determined on the basis of its total travel path,

$$r(t) = c(t_1 - t_0) = c \cdot \Delta t \tag{1}$$

where the time of flight is denoted by (Δt).

The optical route is the aggregate of the lengths passed by the emitted and reflected beams, with the ultimate displacement of the point on the beam surface (δ) considered as half of this journey (r),

$$\delta(t) = \frac{r(t)}{2} = \frac{1}{2} c \cdot \Delta t \tag{2}$$

where (Δt) denotes the time required for the laser beam to travel the complete round-trip path.

If the sensor signals (IR–ToF) are mathematically modeled as the transmitted signal $i_s(t)$and the reflected signal $o_s(t)$, then, according to Eqs. (3) and (4), we obtain

$$i_s(t) = \sin(2\pi f_s t) \tag{3}$$

$$o_s(t) = A \cdot \sin(2\pi f_s t - \theta) \tag{4}$$

$$\theta = \frac{r}{2} = \frac{2\delta}{c} \tag{5}$$

where:

- A is the reflection coefficient,
- c represent the speed of light in air, equal to 299792458 m/s, and
- f_s is the modulation frequency of the transmitted signal $i_s(t)$and the reflected signal $o_s(t)$.

It follows that, once the phase difference $\theta$is measured, the displacement δ between the position of the IR emitter and the point on the beam can be calculated according to Eq. (5). Alternatively, if:

$$\delta = \frac{c}{4\pi f_s} \theta \tag{6}$$

so that,

$$\delta = \frac{1}{2} \frac{c}{2\pi f_s} \theta = \frac{1}{2} c \frac{\theta}{2\pi f_s} = \frac{1}{2} c \cdot \Delta t \tag{7}$$

The displacement range captured by the *Imm_DF_system_2021* spans from 0 to 150 mm, depending on the optical properties of the reflecting surface. For the investigated surfaces and a measurement step of 5 mm, the VL6180X sensor yielded reflected signal levels of 3%, 5%, 17%, and 88%, respectively (Fig. 2b) [13].

Figure 2c demonstrates the sensor response through variations in laser-beam intensity as a function of the color of the reflecting surface. The highest reflectance was observed for the white ceiling, whereas the lowest was recorded for the black wooden board. This contrast was quantified by voltage measurements at 830 points, revealing an average difference of approximately 0.9 V between the two surfaces. The reflected signal intensity decreases exponentially with increasing distance and becomes negligible beyond approximately 130 mm.

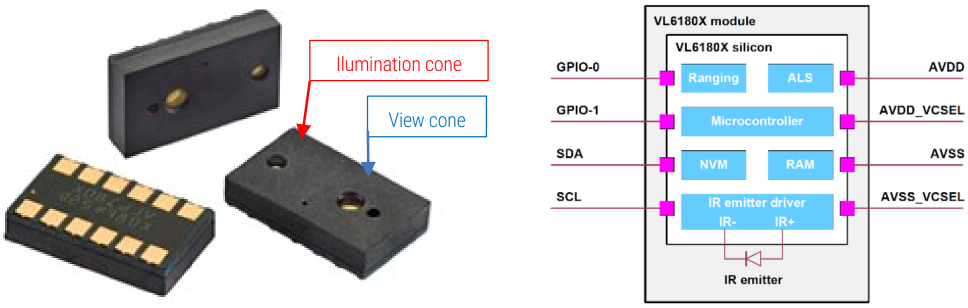

. a) VL6180X module b) VL6180X module

Figure 1. STMicroelectronics Infrared Time-of-Flight proximity sensor (IR-ToF)

The experimental results further show that the VL6180X sensor can reliably detect point displacements irrespective of surface color, including displacements exceeding 100 mm (Fig. 2c), although with slightly larger deviations. Based on these observations, the VL6180X module is well suited for displacement monitoring in the range of 0–100 mm, in accordance with [8]. Moreover, within this interval the sensor response exhibits an approximately linear relationship between the measured distance and the output signal. The influence of high humidity, atmospheric precipitation, and wet surface conditions was not considered in the present investigation.

The original Arduino hardware [10] was developed by the Italian company *Smart Projects*, while Arduino boards are nowadays also manufactured by the American company *SparkFun Electronics*. Arduino (http://arduino.cc/) represents an open-source computing platform. Its hardware core consists of a microcontroller integrated on a simple board equipped with an Atmel AVR processor and appropriate input/output connectors. The "Arduino Genuine" software package includes the C/C++ *Wiring* library, a standard compiler, and a bootloader installed on the board. The development environment is based on the *Processing* platform and uses the *Wiring* programming language, whose syntax and libraries are similar to those of C++, with certain simplifications and modifications. Arduino programs are written in the C/C++ programming language, and each program must define at least two basic functions required for code execution:

- **setup()**—a function that is executed once at startup and is used for initial configuration,
- **loop()**—a function that runs continuously in a loop for the entire duration of board operation.

Arduino Uno (Fig. 3a) is a development board based on the ATmega328 microcontroller, optimized for the integration of a large number of electronic circuits and equipped with 14 digital input/output pins. The board also includes a 16 MHz resonator, a USB interface, a power supply connector, and a reset button. The microcontroller features 32 kB of ISP flash memory, 2 kB of RAM, and 1 kB of EEPROM. Serial communication is supported via the UART, SPI, and I²C interfaces.

Arduino ATmega2560 (Fig. 3b) is a development board based on the ATmega2560 microcontroller and features 54 digital input/output pins (14 of which support PWM), 16 analog inputs, four UART serial interfaces, a 16 MHz crystal oscillator, a USB connection, a power supply connector, an ICSP header, and a reset button. The Arduino Mega 2560 is compatible with most of its versions, such as the ATmega2560 R3, which includes additional SDA and SCL pins located next to the AREF pin. In addition, two new connectors are placed near the RESET pin, one of which is IOREF, allowing the operating voltage of external devices to be matched to the board voltage. This microcontroller model was not used in the present study due to the limited number of monitored measurement points on the beam. However, the ATmega2560 is well suited for displacement monitoring

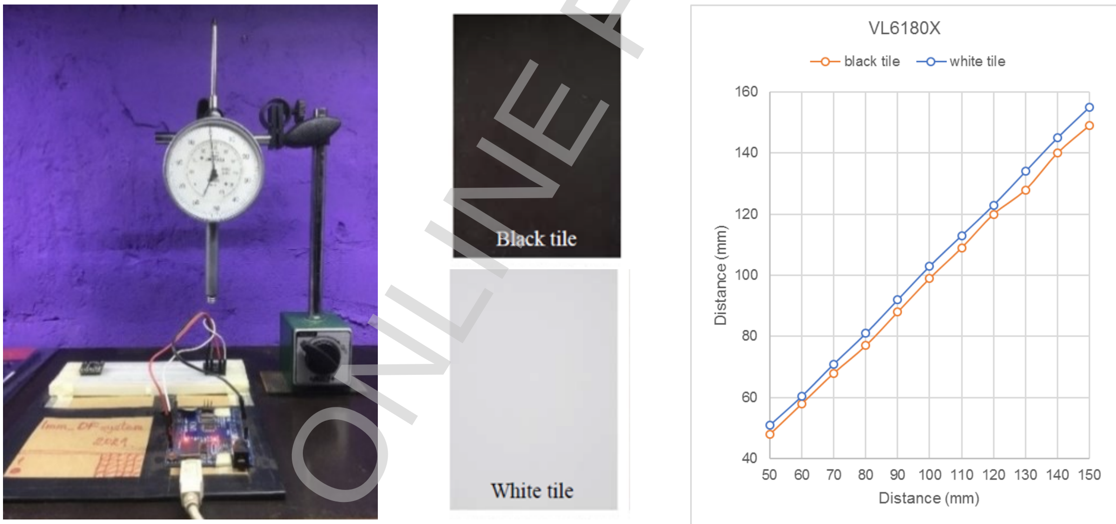

a) b) c)

Figure 2. Experimental setup for sensor VL6180X

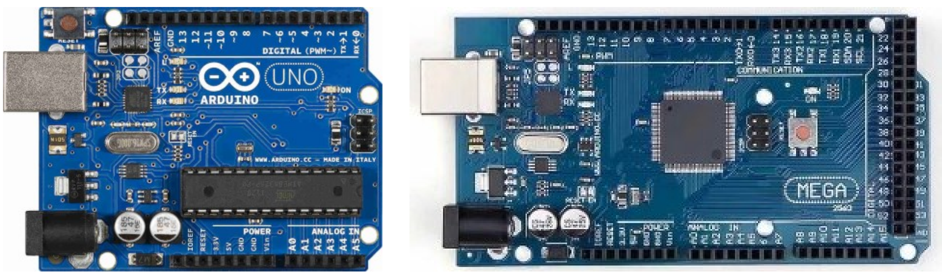

a) b)

Figure 3. a)Arduino UNO b) Arduino ATmega2560

applications in cases where a larger number of points need to be observed simultaneously.

VL6180X (Fig. 1a) designed for proximity and distance measurement to an arbitrary point on an object (Fig.4). Such sensors are widely used today in smartphones, mini-computers (tablets), personal computers, and many other electronic devices. The module incorporates an array of SPAD (Single Photon Avalanche Diode) detectors together with a laser emitter and the associated driving and control circuitry. The emitted laser beam is designed to remain within Class 1 laser safety limits under all operating and foreseeable conditions, provided that the configuration follows the recommendations of STMicroelectronics, including possible and expected fault conditions, in accordance with the IEC 60825-1:2007 standard.

A protoboard (Fig. 5) serves as a basic platform for the assembly and testing of electronic circuits, enabling simple and rapid interconnection of components without soldering. It consists of a regular array of holes, beneath which metal contact strips are bent to form conductive channels. Jumper wires and component leads are inserted into these holes, providing a temporary yet mechanically stable electrical connection with the contact strips.

The metal channels inside the board are referred to as contacts, and the holes within the same column are electrically connected. The long contact rows located at the top and bottom edges of the protoboard are intended for power supply and ground distribution, with most models providing two parallel rows for each. In some protoboard types, the horizontal rows are internally connected, whereas in others they are electrically isolated. The contact strips are manufactured from soft metal and coated with a protective layer to prevent oxidation; however, during long-term use and testing, undesired effects related to contact degradation may still occur.

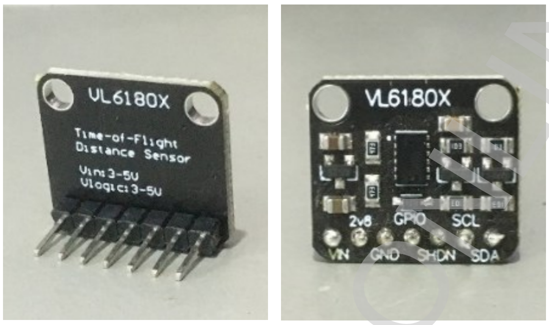

Figure 4. VL6180X-based distance sensor module

Jumper wires (Fig. 6) are used to interconnect connectors and sensors on the protoboard. Wires with a 22 AWG (0.33 mm²) specification, made of solid copper and tin-plated, are recommended. If prefabricated connectors are not attached to the wire ends, the insulation should be stripped over a length of 3/16 to 5/16 in., i.e., approximately 4.8 to 7.9 mm. Excessively short stripped sections may result in poor contact with the spring clips of the board, whereas excessively long stripped sections increase the risk of short circuits. Pliers and tweezers are helpful for inserting and removing wires, particularly when the board is densely populated with components. The usage of different colors for wires is a common technique to improve consistency and readability. However, the number of available colors is usually much smaller than the number of signal paths in a circuit. In practice, certain colors are reserved for power supply and ground (e.g., red, blue, and black), while others are used for signal connections. In some commercially available jumper-wire sets, color coding is also employed to indicate wire length.

3 Materials and methods

Figure 7 illustrates the verification of the vertical deflection at the midspan of the tested beam. The simply supported timber beam, characterized by known geometric and mechanical properties, was subjected to a static load of m = 114 kg. The vertical displacement at the bottom fiber in the midspan section was monitored simultaneously using the proposed *Imm_DF_system_2021* and a reference *Insize* mechanical dial gauge with a resolution of 0.01 mm. In addition, the time-dependent loading of the beam was investigated under both short-term loading (approximately 1 h) and long-term loading (approximately 6 h). After these two loading phases, unloading was performed and a technical zero was re-established, enabling the registration of residual displacements over a 24-hour period following load removal. The experimental program did not include monitoring of stiffness variation. A quantitative comparison of the displacements measured by the two systems is presented in Table 1. It should be emphasized that an integrated loading system was employed, allowing the static load to remain applied to the beam even after the displacement readings obtained by the dial gauge had been recorded. It was observed that the mechanical dial gauge exhibited a smaller pointer return, resulting in a displacement value different from the previous one, which can be attributed to rheological effects in the beam material.

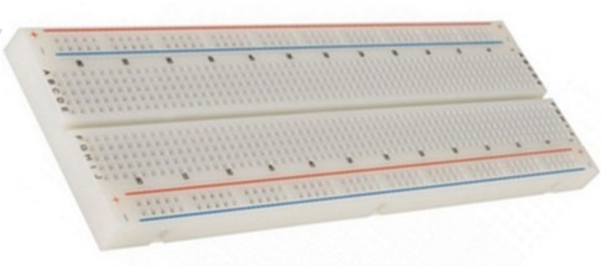

Figure 5. 830-point breadboard

Figure 6: Jumper wires M-M

During the experiment, all measured displacements were controlled using the analytical solution for the case of a concentrated load applied at midspan, i.e., at the location of the selected measurement point on the beam,

$$y_{max} = \frac{1}{48} \cdot \frac{Pl^3}{EI} \quad y_{max} = 38.78\,\text{mm} \tag{8}$$

- while the rotations of the end cross-sections of the beam are,

$$\alpha = \beta = \frac{1}{16}\frac{Pl^2}{EI} \quad \alpha = \beta = 0.07458 \text{ [rad]} \tag{9}$$

On the other hand, the analytical expressions for the case of a uniformly distributed load provide the displacement distribution along the beam,

$$y(z) = \frac{1}{24}\frac{pl^4}{EI}\left[\frac{z}{l} - 2\left(\frac{z}{l}\right)^3 + \left(\frac{z}{l}\right)^4\right] \tag{10}$$

- the maximum displacement occurs at the midspan of the beam,

$$y_{max} = y_{(l/2)} = \frac{5}{384}\frac{ql^4}{EI} \tag{11}$$

- while the rotations of the beam end cross-sections are,

$$\alpha = \beta = \frac{1}{24}\frac{ql^3}{EI} \tag{12}$$

The adopted beam model is simply supported, with a pinned support at one end and a roller support at the other, over a total span of L = 156 cm. The beam is made of softwood of strength class II and is finished with a high-quality protective and decorative coating (Figs. 9-2, 9-3, 9-4). It has a rectangular cross-section with dimensions b/h = 190 × 25 mm (Fig. 4a). The material density, as well as the static and dynamic moduli of elasticity, was determined experimentally. The selected cross-sectional dimensions were chosen in an appropriate proportion with respect to the beam span,

$$h = \frac{L}{62.5} \tag{13}$$

$$b = \frac{L}{8.2} \tag{14}$$

where is: h – beam depth, b – beam width, and L – beam span.

The cross-sectional depth was selected in accordance with Eq. (13) to enable testing of the beam model under a relatively low ballast load. This choice ensured stable structural behavior and satisfied the self-stability criterion of the system. Moreover, a verification analysis performed with respect to the serviceability limit state indicates that, under the applied static test load (total ballast), the beam exhibits vertical deflection,

$$\frac{L}{40.22} = \delta = 3.878 \text{ cm}$$

Accordingly, based on the technical specifications given, the constructed physical beam model (Fig. 9) represents a structurally and kinematically rigid, statically determinate system of a simply supported beam. The static loading in the experiment was provided by rolled steel U100 sections with a total mass of m = 114 kg, applied in four equal loading stages of m = 28.5 kg each (Fig. 2–5). To verify the experimental results in the theoretical analysis, the total static test load ("ballast") was represented by an equivalent static model consisting of a single vertical concentrated force applied at the midspan.

3.1 Integrated static system

The integrated static loading system was modeled as a variable-mass system and implemented through six successive loading stages. In the initial ("zero") stage, the beam specimen was mounted on the test frame (Fig. 9-1), and both measuring devices were accurately positioned and fixed at the midspan on the bottom fiber of the beam. An initial reference reading was obtained using the dial gauge. Subsequently, the MS Excel environment with the PLX-DAQ (Release 2.0) VB module was launched (Fig. 9-7), and the second measuring system was activated (Fig. 9-8). In the first loading stage, a mass of m = 28.5 kg was applied (Fig. 9-5), and the corresponding deflection was recorded. In the second stage, the total applied mass was increased to m = 57 kg; in the third stage, to m = 85.5 kg; and in the fourth stage, to m = 114 kg, with displacement readings taken after each load increment. In the final unloading stage, the entire ballast mass of 114 kg was removed, the residual deflection was measured, and all recorded data were stored in *.xlsx* format.

This experimental procedure enabled continuous monitoring of beam deflection as a function of both time and load level while providing synchronized measurements from the two independent measurement systems at identical time instants. Such an approach allowed a direct comparison between the systems and clearly demonstrated the advantages of the proposed monitoring system (Fig. 2-8) with respect to the reference dial gauge (Fig. 2-9). The

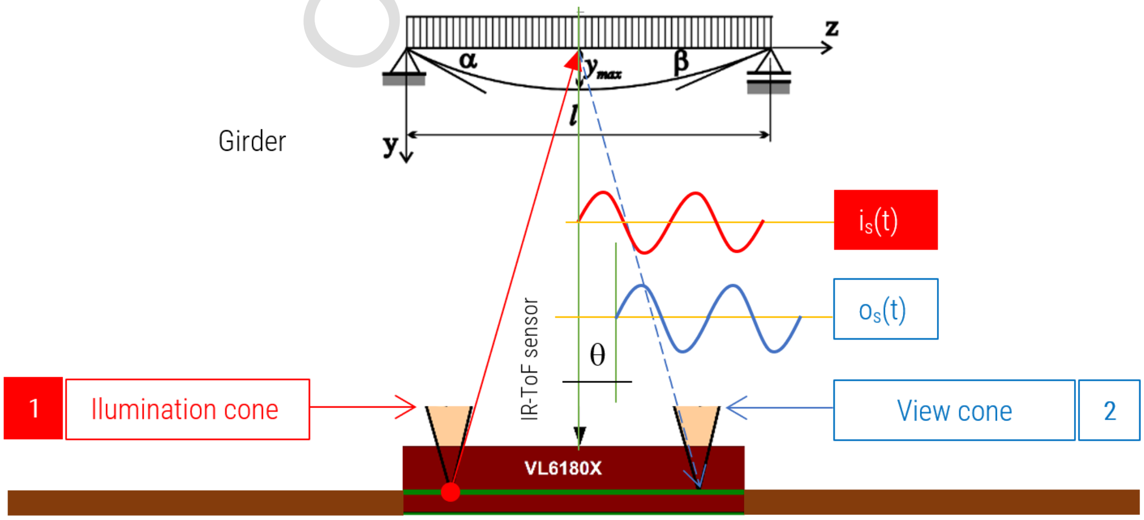

Figure 7. Principle of operation of the sensor for displacement measurement

primary objective was to perform displacement monitoring using the proposed system, with the conventional instrument serving as a validation tool. Particular attention was paid to strict adherence to the experimental protocol defined in the test program, especially considering the duration of individual loading stages and the technical limitations of the data acquisition system, including memory capacity, storage space, and computer hardware performance.

3.2 Numerical modeling and analysis

The numerical analysis was carried out using the commercial software AxisVM9 with a two-dimensional line-beam model. The beam was discretized into a finite element mesh consisting of 21 nodes and 20 beam elements (Fig. 8). The material properties were determined experimentally and are given as: $E = 9450$ MPa, $\nu = 0.20$, and $\rho = 530\ \text{kg/m}^3$.

The structural response for the individual loading stages, as well as for the total applied load, was evaluated within the framework of first-order finite element theory. First, the vertical displacement distribution caused by a concentrated force equivalent to the ballast in the first loading stage, $P_1 = 9.807 \times 28.5 = 279.50$ N, was computed and compared with the experimentally measured deflection. The vertical displacement at the midspan of the beam obtained from this analysis was $\delta = 9.591$ mm (Fig. 9-6). Finally, the total static test load applied to the beam model was $P_u = 114\ \text{kg} \times 9.807\ \text{m/s}^2 = 1117.99\ \text{N} \approx 1.12$ kN, which resulted in a midspan vertical displacement of $\delta = 37.623$ mm (Fig. 8).

4 Experimental modeling, analysis and results

The experimental results of the beam vertical displacements were collected on the physical model according to the scheme shown in Fig. 11 during two monitoring periods. The first period covered the interval from 1 January 2023 to 1 July 2023, comprising a total of 150 tests. The second period extended from 15 April 2025 to 30 October 2025 and also included 150 tests. According to the test program, a total of 1000 midspan displacement tests were planned to determine the technical (instrumental) error of the proposed measurement system [17].

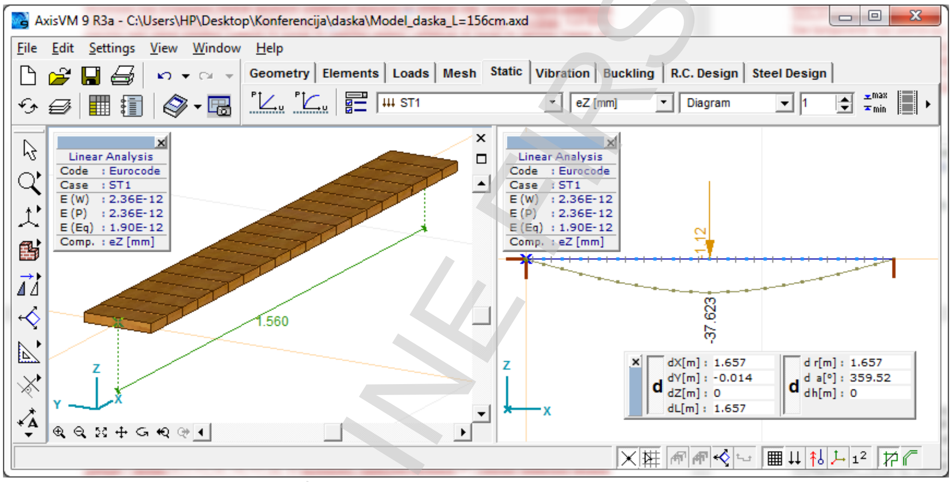

Figure 8. Numerical modeling and simulation of the beam model

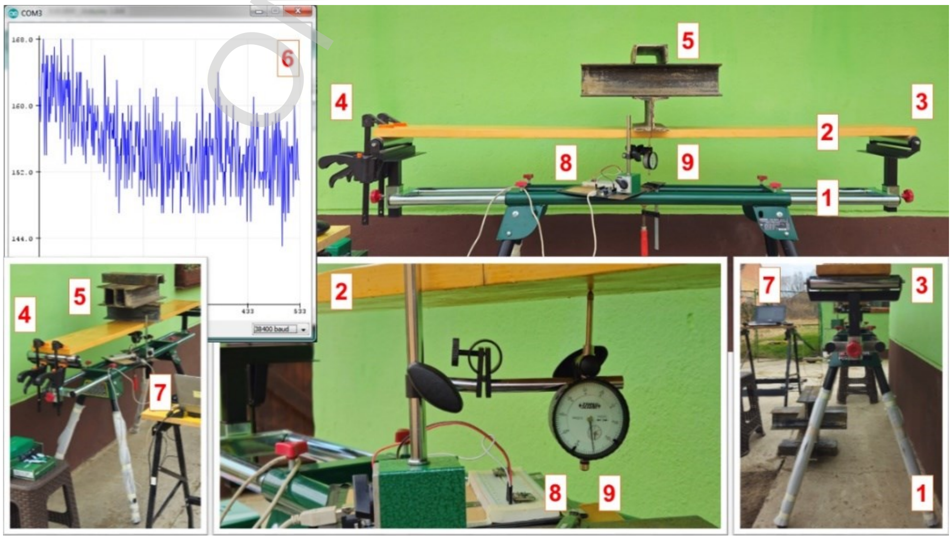

Figure 9. Experimental system: 1 – test frame, 2 - support, 3 - movable bearing, 4 - fixed bearing, 5 - ballast, 6 - deflection monitoring system, 7 - laptop, 8 - Imm_DF_system_2021, 9 - mechanical dial gauge Insize

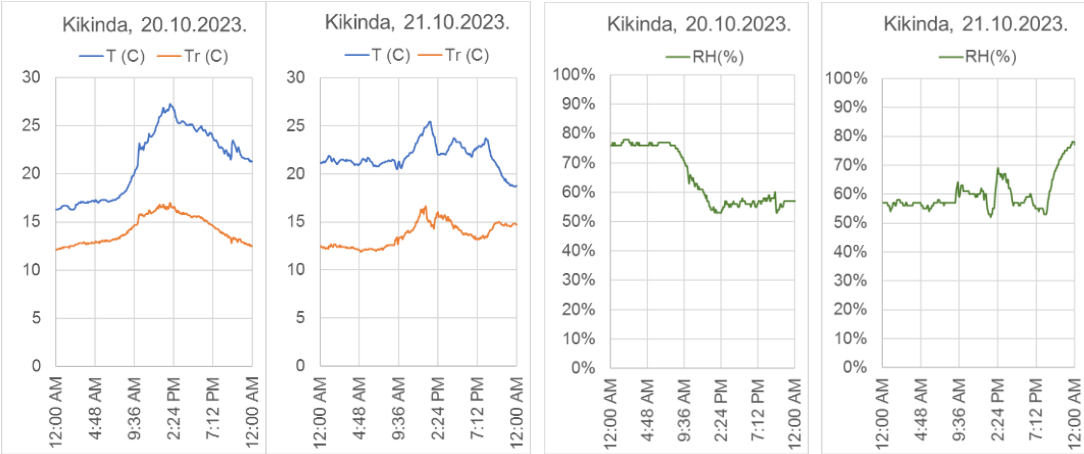

a) b) c) d)

Figure 10. Meteorological data: air temperature and relative humidity recorded in Kikinda, Republic of Serbia

The first 100 displacement measurements were analyzed using statistical methods and, with respect to the mean value, demonstrated the highest accuracy at the initial measurement stage. Based on these results, an experimental campaign was carried out on a simple timber beam model during the period from 20 to 21 October 2023. The *in situ* specimen was subjected to a static test load under actual environmental conditions of air temperature and relative humidity (Figs. 10a–d). Subsequently, an additional 50 tests were performed, thereby completing the first validation phase of the second displacement monitoring system (Fig. 9-8). The preliminary evaluation indicates that the measurement accuracy of the proposed system, relative to the mean displacement, is approximately 0.04, i.e., practically 0%.

In the second testing period (2023–2025), which included a further 150 tests, the estimated measurement uncertainty was slightly higher and amounted to approximately 0.026 (≈0%). The experimental program is therefore planned to be extended to a total of 1000 measurements in order to determine the system accuracy in accordance with the theoretical framework presented in [17], pp. 9–11. The differences observed between the two testing periods can be attributed to the rheological behavior of wood, particularly to mechano-sorptive effects. Figure 11 presents the schematic layout of the beam model and the measurement locations, showing three VL6180X sensors mounted on a protoboard and connected to a laptop via a USB interface.

The midspan displacement data were saved in *.xlsx* format after each loading stage and then imported into MATLAB 2021a for further analysis. Because of their volume, the complete source codes are not included in this paper. Columns D–E–F present representative displacement records from all three measurement locations during the fourth loading stage (Fig. 12). The second worksheet, entitled “Graph,” shows the time histories of midspan deflection for tests lasting 1 h and 6 h (Figs. 13–15). The tests were performed independently: the first on 07 April 2023 between 13:37:14 and 14:37:16 (approximately 1 h, 3561 samples), and the second on 08 April 2023 between 13:59:55 and 19:34:01 (approximately 6 h, 19817 samples). The sampling interval was 1000 ms (1 Hz) and can be modified in the Arduino application. Increasing the number of samples did not improve the accuracy of the measurements but only increased the required memory capacity.

In the experimental program, two measurement systems were employed. The first, shown in Fig. 9-9, served as a reference system and consisted of a magnetic stand equipped with a mechanical *Insize* dial gauge. The second system, *Imm_DF_system_2021* (Fig. 9-8), was used for continuous monitoring of the midspan deflection. This system incorporates a VL6180X sensor, which emits a laser beam with a wavelength of 820 nm and measures the time required for the beam to be reflected from the beam surface and return to the photodiode. Analysis of the reflected signal allows the surface condition of the beam to be assessed and enables discrimination between dry and moist states. The effects of frozen surfaces, as well as the presence of snow and ice, were not considered in the present study.

4.1 Spectral analysis

Spectral analysis is used to study the frequency content of a signal. According to Parseval’s theorem, the total energy of a signal is the same in the time domain and in the frequency domain [19]. The concept of a spectrum was first illustrated in the seventeenth century by Isaac Newton (1643–1727) through his experiments on the refraction of sunlight using a glass prism. He showed that white light is composed of a range of colors, each associated with a specific wavelength. This observation introduced the concept of a spectrum.

The mathematical foundations of spectral analysis were later established by Jean-Baptiste Joseph Fourier (1768–1830), who is regarded as the founder of harmonic analysis. In experimental mechanics, the transformation of a displacement signal from the time domain to the frequency domain is performed by Fourier analysis, most commonly using the Fast Fourier Transform (FFT). The inverse operation, which reconstructs the time-domain response from its frequency components, is known as the inverse Fast Fourier Transform (iFFT) or Fourier synthesis (Figs. 16–19).

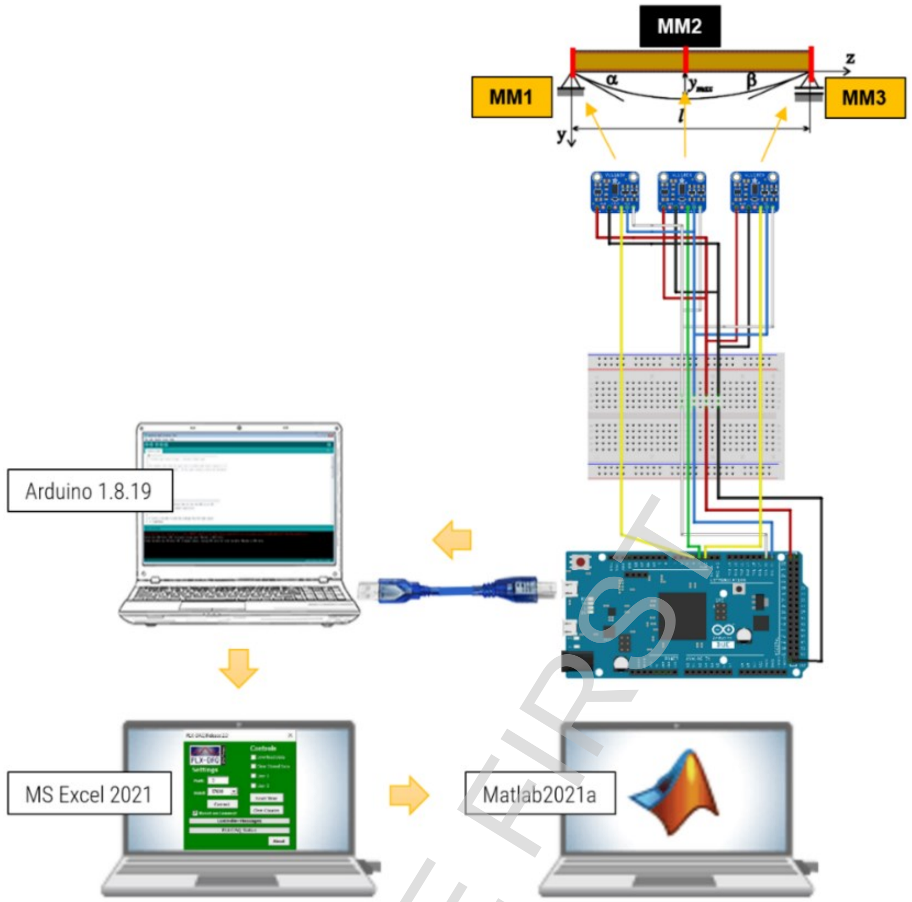

Figure 11. Schematic layout of the Imm_DF_system_2021 monitoring system

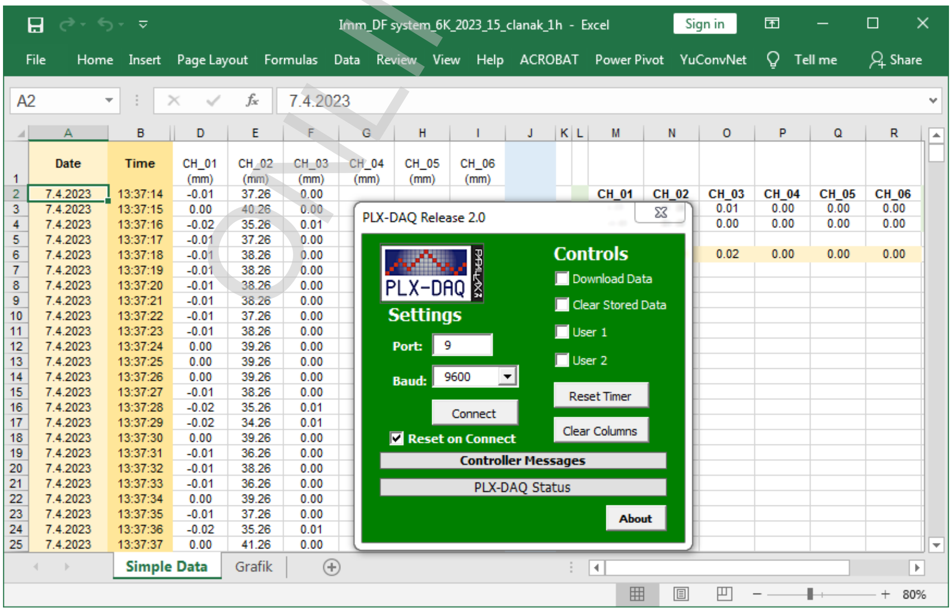

Figure 12. Automatic recording and real-time visualization of displacement signals at measurement points MM1 (CH_01), MM2 (CH_02), and MM3 (CH_03)

Identifying the components in the system response and evaluating their relevance necessitates the implementation of the Fourier transform [18–23].

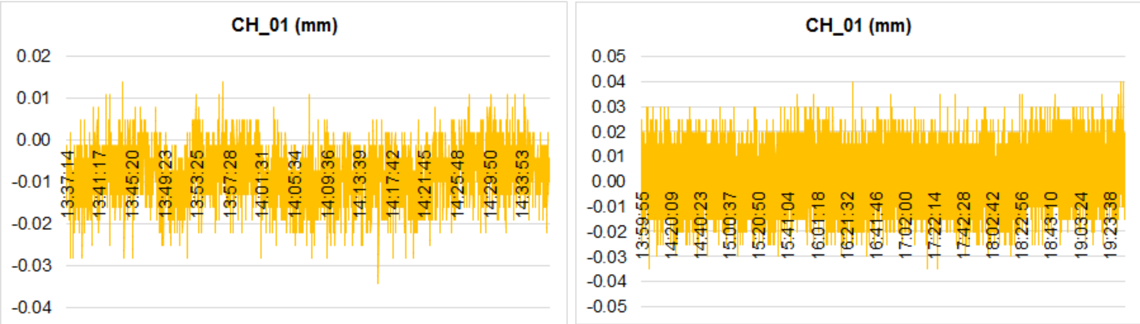

Figure 13. Displacement monitoring at point MM1 during four loading phases: short-term test (1 h, left) and long-term test (6 h, right)

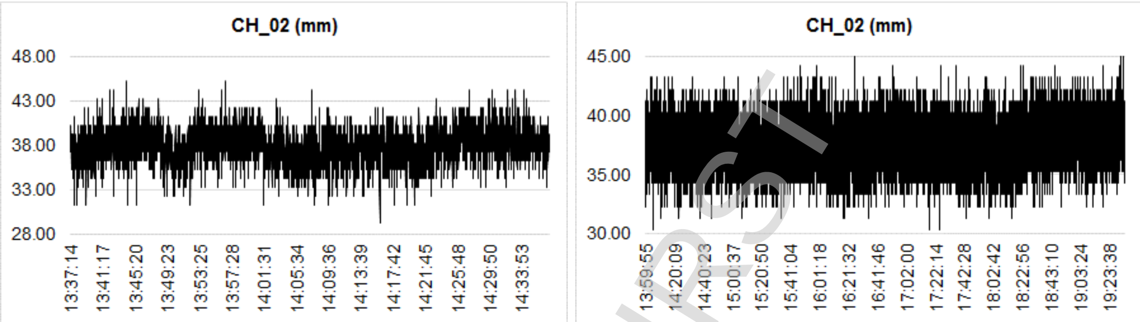

Figure 14. Displacement monitoring at point MM2 during four loading phases: short-term test (1 h, left) and long-term test (6 h, right)

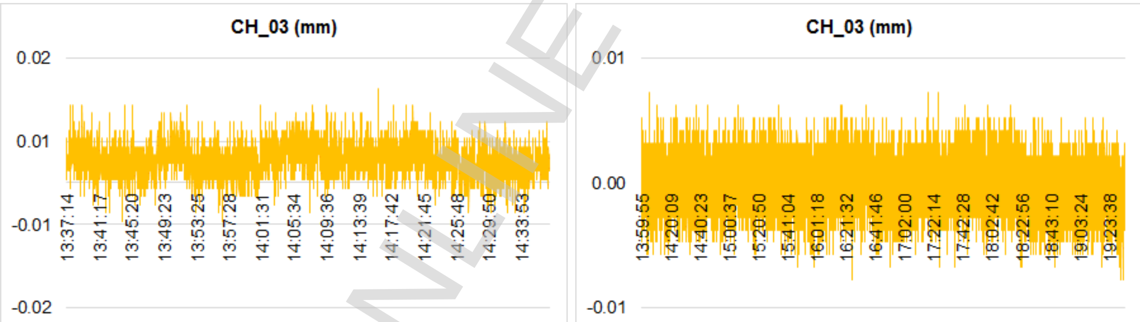

Figure 15. Displacement monitoring at point MM3 during four loading phases: short-term test (1 h, left) and long-term test (6 h, right)

4.1.1 DFT - Discrete fourier transformation

The Discrete Fourier Transform (DFT) is used to transfer a signal from the time domain to the frequency domain and enables the identification of dominant harmonic components in the system response. In the case of beam displacement signals, the DFT allows the decomposition of a discrete measurement sequence into a set of sinusoidal components with different frequencies, amplitudes, and phases. The DFT coefficients define the exact frequency spectrum of a discrete signal and are based on the assumption of periodic extension with a period of MMM samples. If the length of the original signal is less than or equal to MMM, the periodic extension coincides with the original signal, and the spectrum can be uniquely reconstructed. Otherwise, spectral overlap (aliasing) occurs, resulting in a loss of information. For a periodic discrete signal, the sequence of samples can be represented as a linear combination of a finite number of complex sinusoids, where the number of harmonics corresponds to the number of samples within one period. The discrete Fourier series can then be written in the following form:

$$x_n = \sum_{m=-\infty}^{+\infty} x_m \delta_{(n-m)} \tag{15}$$

When the signal is periodic, it can be represented as a linear combination of a finite number of complex sinusoids. In this case, the number of complex sinusoids corresponds to the number of samples within one period of the signal, as given by the following expression:

$$x_n = \sum_{n=0}^{M-1} X_k e^{jk\omega_0 n} \tag{16}$$

where,

$$\omega = k\omega_0 = \frac{2\pi k}{M} \tag{16a}$$

$$\frac{k}{M} \cong f, \quad n \cong t \tag{16b}$$

then the discrete Fourier series takes the form,

$$X_k = \frac{1}{M}\sum_{n=0}^{M-1} x_n e^{-jk\omega_0 n} \tag{17}$$

The DFT of the displacement signal can be expressed either in terms of continuous series components or in the form of a discrete series. When the real (trigonometric) representation is used, two separate integrals are evaluated: one corresponding to the correlation of the signal with a cosine function (Eq. 18) and the other to the correlation with a sine function (Eq. 19). These two operations yield two real-valued coefficients in the frequency domain. Consequently, the spectral content of the signal is obtained by performing correlation with both cosine and sine basis functions, resulting in two real Fourier coefficients for each frequency component,

$$X_a(f) = \int_{-\infty}^{+\infty} x(t)\cos(2\pi f t)\, dt \tag{18}$$

$$X_b(f) = \int_{-\infty}^{+\infty} x(t)\sin(2\pi f t)\, dt \tag{19}$$

On the other hand, when the complex notation is adopted, the signal transformation is reduced to a single integral (Eq. 20) with a complex-valued coefficient in the frequency domain,

$$X(f) = \int_{-\infty}^{+\infty} x(t) e^{-j(2\pi f)t} dt \tag{20}$$

Thus, the transformation that maps a finite-length signal $x_n$into its spectral representation $X_k$is referred to as the Discrete Fourier Transform (DFT) of the signal x_n, and it is expressed in the following series form,

$$X_k = X(\omega) = X_{\left(\frac{2\pi}{M}k\right)} = \sum_{n=0}^{M-1} x_n e^{-j\frac{2\pi k}{M}n} \quad (k = 0,1,2,\dots,M-1) \tag{21}$$

$$b_n = \frac{2\pi k}{M}n \tag{21a}$$

If the summation in Eq. (21) is expanded, it yields a sum of the signal samples multiplied by complex exponential coefficients.

$$X_k = x_0 e^{-b_0 j} + x_1 e^{-b_1 j} + \dots + x_n e^{-b_{N-1} j} \tag{22}$$

Using Euler's formula,

$$e^{jx} = cosx + jsinx$$

we obtain the expanded trigonometric series in the frequency domain in the form:

$$X_k = x_0[\cos(-b_0) + jsin(-b_0)] + \cdots \tag{23}$$

that is, in the trigonometric form given by Eq. (23), the real and imaginary parts of the frequency spectrum are given by,

$$X_k = \sum_{n=0}^{M-1} x_n\left[\cos\left(\frac{2\pi k}{M}n\right) - jsin\left(\frac{2\pi k}{M}n\right)\right] \tag{24}$$

Thus, a complex number is obtained,

$$X_k = A_k + B_k j$$

and, by applying the Pythagorean theorem, the amplitude and phase angle of the displacement of the point on the beam are determined.

$$A = \sqrt{{A_k}^2 + {B_k}^2} \qquad \theta = arctg\frac{B_k}{A_k}$$

Example: If a recorded signal has the characteristics $f = 1$Hz and $A = 1$, with a total number of samples $M = 8$and a sampling frequency $f_s = 8$Hz, then the corresponding discrete signal sequence is given by:

$$x_0 = 0, x_1 = 0.707, x_2 = 1.0, x_3 = 0.707, x_4 = 0, x_5 = -0.707, x_6 = -1.0, x_7 = -0.707$$

The first ordinate in the frequency domain, according to Eq. (22), is:

$$X_1 = 0e^{\frac{-j2\pi\cdot 1}{8}\cdot 0} + 0.707e^{\frac{-j2\pi\cdot 1}{8}\cdot 1} + 1.0e^{\frac{-j2\pi\cdot 1}{8}\cdot 2} + +0.707e^{\frac{-j2\pi\cdot 1}{8}\cdot 3} + \cdots$$

or,

$$X_1 = 0[\cos(0) + jsin(0)] + 0.707\left[\cos\left(-\frac{\pi}{4}\right) + jsin\left(-\frac{\pi}{4}\right)\right] + +1.0\left[\cos\left(-\frac{\pi}{2}\right) + jsin\left(-\frac{\pi}{2}\right)\right] + \cdots$$

finally, the ordinate in the frequency domain is,

$$X_1 = 0 + (0.5 - 0.5j) + (-j) + (-0.5 - 0.5j) + (0.5 - 0.5j) + +(-j) + (-0.5 - 0.5j) = -4j$$

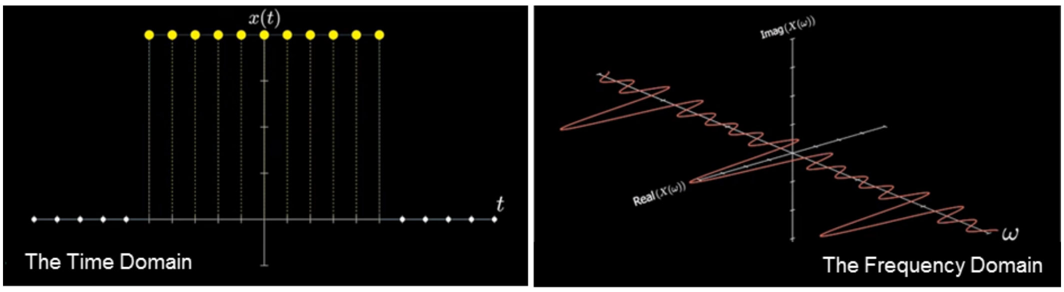

Figure 16. DFT of a discrete displacement signal

Second ordinate in the frequency domain according to (22),

$$X_2 = 0e^{\frac{-j2\pi\cdot 2}{8}\cdot 0} + 0.707e^{\frac{-j2\pi\cdot 2}{8}\cdot 1} + 1.0e^{\frac{-j2\pi\cdot 2}{8}\cdot 2} +$$

$$+0.707e^{\frac{-j2\pi\cdot 2}{8}\cdot 3} + \cdots$$

or,

$$X_2 = 0\left[\cos\left(-\frac{\pi}{4}\right) + j\sin\left(-\frac{\pi}{4}\right)\right] +$$

$$+0.707\left[\cos\left(-\frac{\pi}{2}\right) + j\sin\left(-\frac{\pi}{2}\right)\right] +$$

$$+1.0[\cos(-\pi) + j\sin(-\pi)] + \cdots$$

finally, the ordinate in frequency domain is $X_2 = 0$

Finally, all Fourier coefficients in the frequency domain were determined,

$$X_0 = 0, X_1 = 0 - 4j,$$

$$X_2 = 0, X_3 = 0, X_4 = 0, X_5 = 0, X_6 = 0, X_7 = 0 + 4j$$

If the frequency components above the Nyquist limit are removed in the frequency domain, and the remaining components are then doubled in magnitude, the resulting Fourier coefficients in the frequency domain are obtained as follows,

$$X_0 = 0, X_1 = 0 - 8j, X_2 = 0, X_3 = 0$$

The DFT represents the Fourier transform evaluated at a number of equally spaced frequency points equal to the number of samples in the discrete signal. The number of elements within one period (M) may be greater than the length of the original signal (x_n). The highest frequency component obtained in the DFT spectrum, $f_{\max} = f_{\mathrm{nyq}}$, is referred to as the Nyquist frequency,

$$f_{max} = f_{nyq} = \frac{f_s}{2} \tag{25}$$

where (fs) denotes the sampling frequency of the displacement signal.

Finally, from Eqs. (21) and (21a), the inverse DFT given by Eq. (26) is readily obtained, yielding a series representation of a periodic signal and thereby confirming the successful reconstruction of the original signal,

$$x_n = \frac{1}{M}\sum_{k=0}^{M-1} X_{\left(\frac{2\pi}{M}k\right)} e^{\frac{j2\pi k}{M}n} \qquad (n = 0,1,2,\ldots,M-1) \tag{26}$$

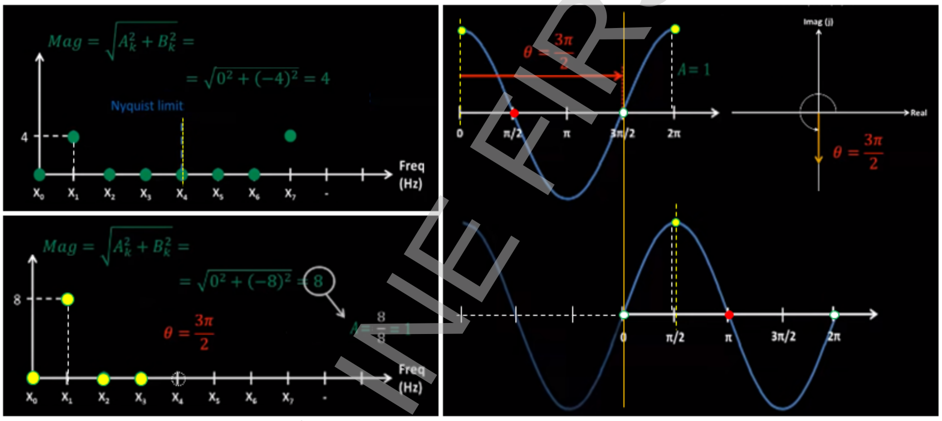

Figure 17. Example of a signal in the frequency domain obtained by DFT

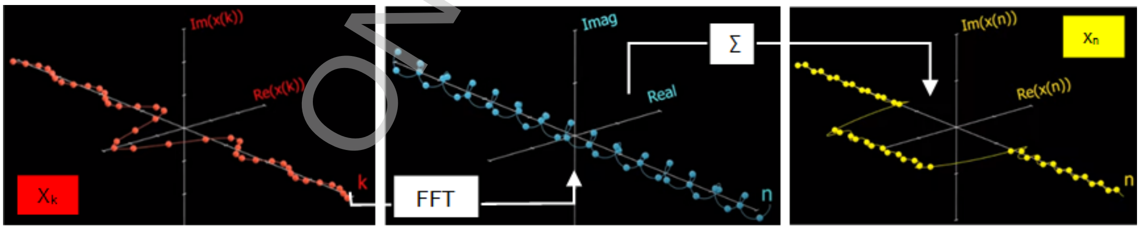

a) b) c)

Figure 18. Flow diagram of the inverse discrete Fourier transform (iDFT) applied to the displacement signal

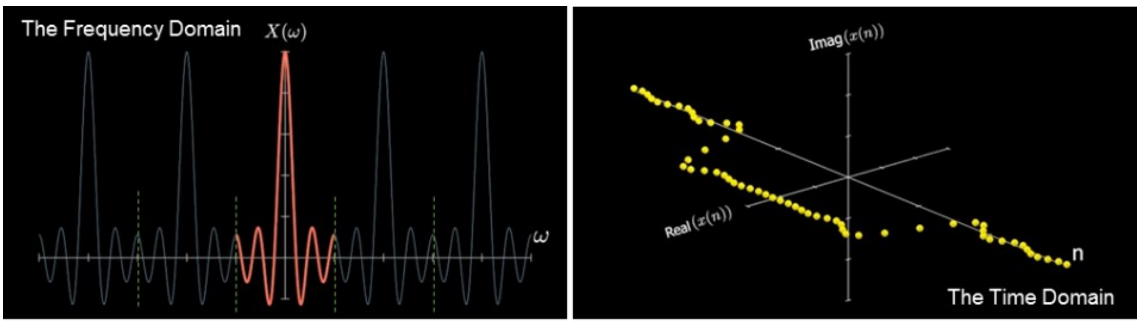

Figure 19. Flow diagram of the inverse Fourier transform (iDFT) for the continuous displacement signal

On the other hand, the iDFT in integral form is given by Eq. (27).

$$x(n) = \frac{1}{2\pi}\int_{-\pi}^{\pi} X(\omega)e^{j\omega n}d\omega \qquad (27)$$

4.1.2 DFT Analysis of the girder displacement signal

In the experiment, all displacement monitoring results were recorded in the time domain with a sampling interval of ΔT = 1000 ms (1 s). Subsequently, the Discrete Fourier Transform (DFT) was applied to both recorded signals, and the raw signals were filtered using a low-pass Butterworth filter. The filtered signals were then further analyzed by means of the Fast Fourier Transform (FFT). In both the DFT and FFT procedures, the frequency content and amplitude of the displacement response were examined for short-term and long-term behavior under static test loading applied in four loading phases. Numerical simulations indicate that the FFT is computationally more efficient than the DFT. Therefore, the results of the DFT simulations are first presented in Figs. 16–18, followed by the filtering of the raw measurement signals, after which the FFT analysis of the filtered signals is shown in Figs. 20–23.

4.1.3 Butterworth low-pass filtering of displacement signals

Filters can be classified into several categories [24–27]: low-pass, high-pass, band-pass, and band-stop filters. They can be implemented using either analog or digital components. The main objective of signal filtering is to suppress unwanted disturbances and noise and to reduce the influence of signal components that are not relevant for the interpretation of the structural response.

Butterworth demonstrated in [24] that a low-pass filter can be defined with a cutoff frequency normalized to 1 rad/s, for which the corresponding frequency response (i.e., the amplitude gain) is given by:

$$G(\omega) = \frac{1}{\sqrt{1+\omega^{2n}}} \qquad (28)$$

where:

ω is the angular frequency (rad/s) and n is the filter order, equal to the number of poles of the filter (which corresponds to the number of reactive elements in a passive filter).

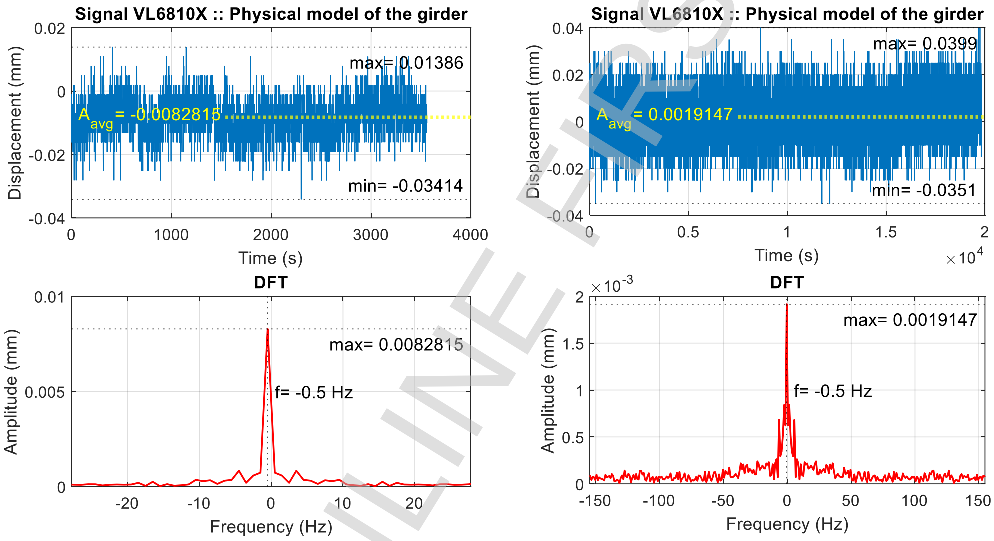

Figure 20. MM1 – four stages displacement monitoring: 1h - left, 6h – right

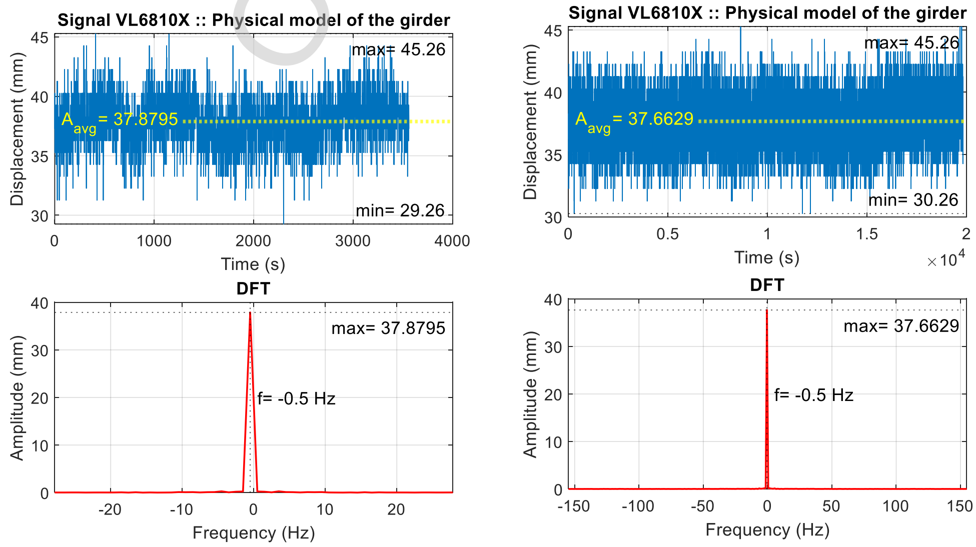

Figure 21. MM2 - displacement monitoring in four phases: 1h - left, 6h – right

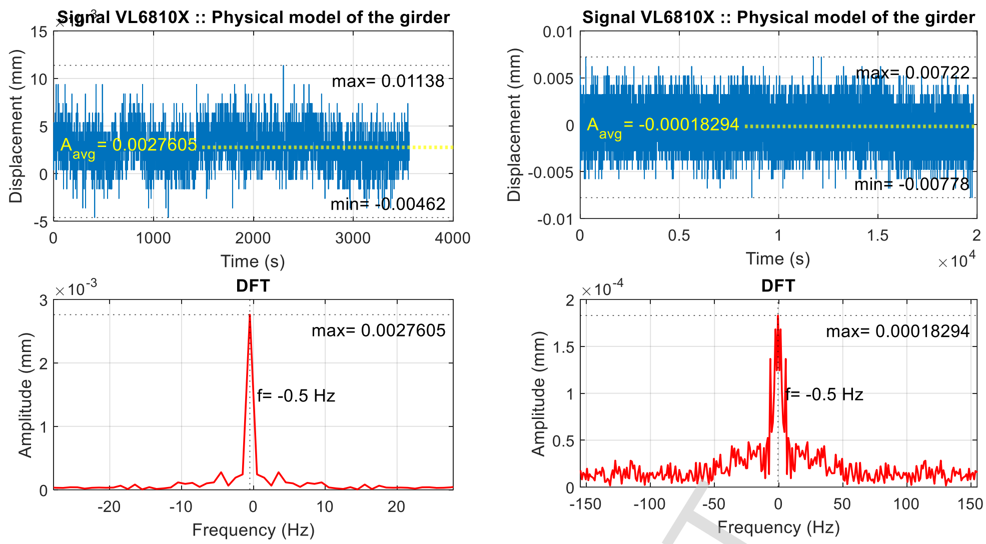

Figure 22. MM3 - displacement monitoring in four phases: 1h - left, 6h - right

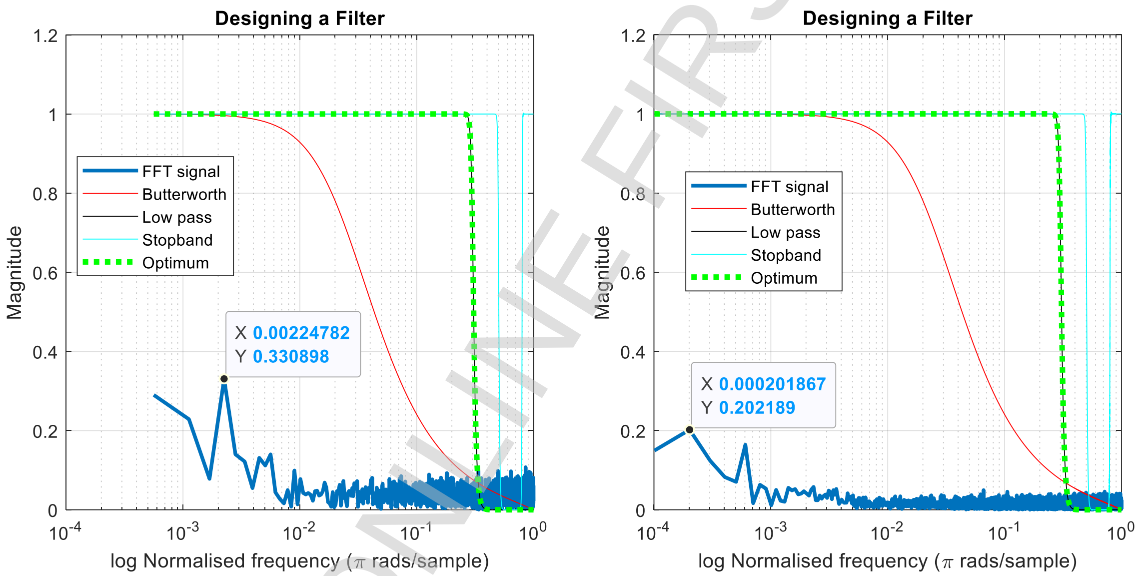

Figure 23. Butterworth low-pass filtered displacement signal at MM2 during four loading phases: short-term test (1 h, left) and long-term test (6 h, right)

For $\omega = 1$, the magnitude response of this type of filter in the passband is equal to $1/\sqrt{2} \approx 0.7071$, which corresponds to one-half of the signal power, i.e., a −3 dB amplitude level. In his original work [24], Butterworth considered only filters with an even number of poles. An example of a first-order Butterworth low-pass filter is shown in Fig. 23, where the corresponding amplitude–frequency response is illustrated,

$$F(s) = \frac{V_0(s)}{V_1(s)} = \frac{1}{1+2s} \tag{29}$$

According to Eq. (29), the magnitude of the frequency response, i.e., the gain, is described by a first-order transfer function (polynomial),

$$G^2(\omega) = |F(j\omega)|^2 = F(j\omega) \cdot F(j\omega) = \frac{1}{1+\omega^{2\cdot 1}} \tag{30}$$

where the phase shift is given by,

$$\theta(\omega) = \arg H(j\omega) \tag{31}$$

The application of the DFT combined with the simulation of a first-order “Butterworth low” filter to the system response obtained in the experiment is presented in Figs. 20–22. One of the main objectives of the analysis is illustrated in the form of a block diagram, modeled for simulation purposes in the MATLAB 2021a environment. However, due to their extent, these results are not presented in full in this paper.

On the other hand, a representative portion of the independently developed MATLAB 2021a program code is provided in Eqs. (32) and (33). By applying the data-processing algorithm (Figs. 23 and 24–26), the procedure for simulating the first-order Butterworth low-pass filter (with filter order (b = 1)) is implemented and integrated into the overall numerical analysis.

$$y=filter(b,a,s) \quad (32)$$

$$[b,a] = butter(1,0.025,'low') \quad (33)$$

Based on the complete set of records from 2023, which include measurements of the midspan displacement in the fourth loading phase obtained both by the mechanical *Insize* dial gauge (with a resolution of 0.01 mm) and by the recorded "raw" and "filtered" displacement signals summarized in Table 1, a consolidated overview of the results is provided.

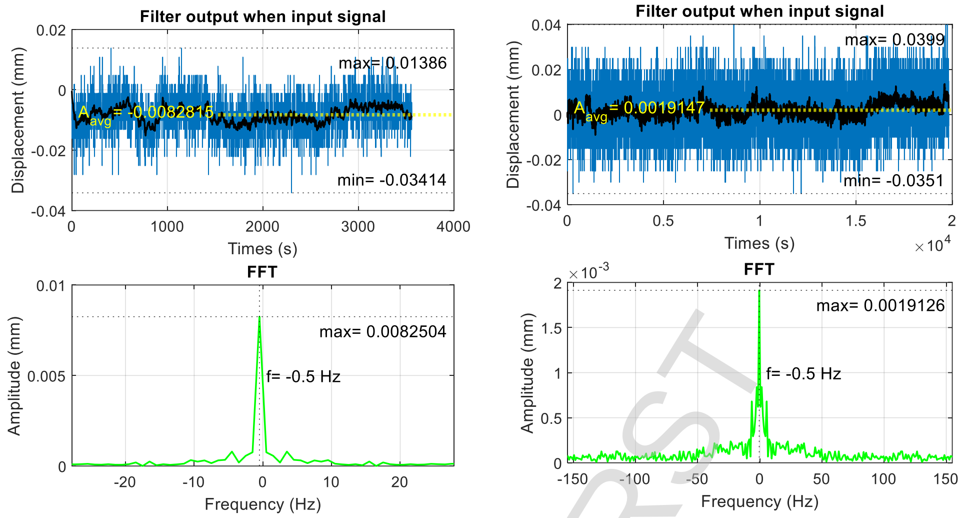

Figure 24. MM1 – Filtered displacement response of the girder during four loading phases: short-term test (1 h, left) and long-term test (6 h, right)

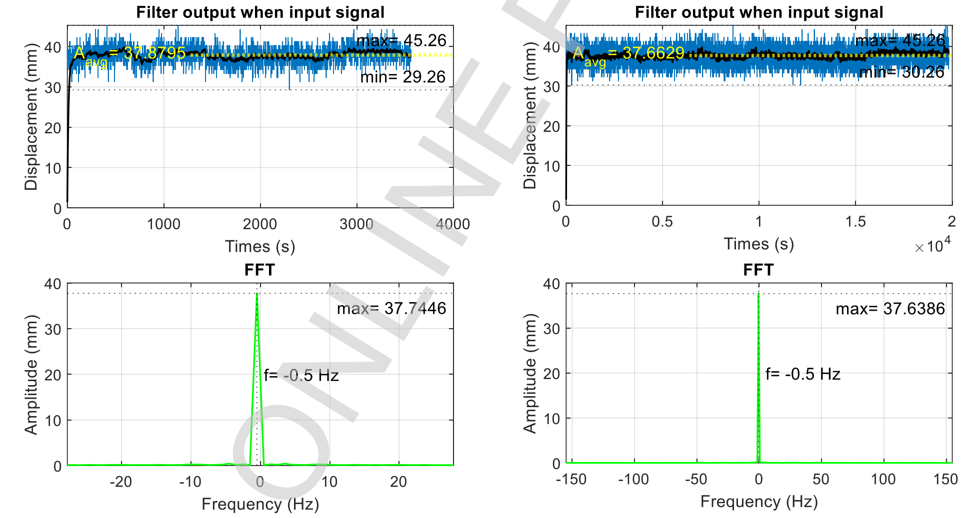

Figure 25. MM2 – Filtered displacement response of the girder during four loading phases: short-term test (1 h, left) and long-term test (6 h, right)

Table 1. Midspan displacement of the girder model at the fourth loading stage.

4 phase	Analytical	MKE	Experiment			
			1h		6h	
			measured value	filtered value	measured value	Filtered value
	(1)	(2)	(3)	(4)	(5)	(6)
Displacement (mm)	38.78	37.623	37.8795	37.7446	37.6629	37.6386
Difference	(1-2)	(2-3)	(2-4)	(2-6)	(3-5)	(4-6)
(%)	3.08	-0.68	-0.32	-0.04	0.58	0.28

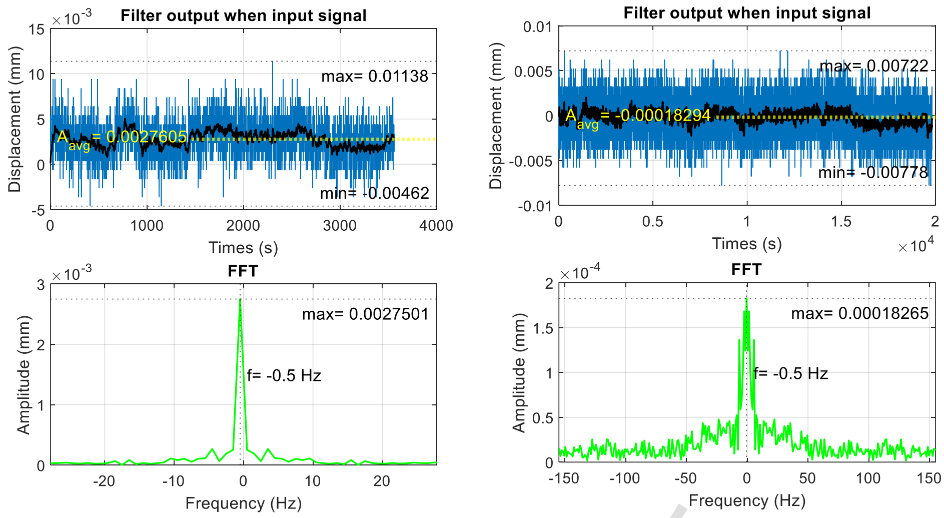

Figure 26. MM3 – Filtered displacement response of the girder during four loading phases: short-term test (1 h, left) and long-term test (6 h, right)

5 Discussion

By monitoring the displacement of the midspan point of a timber beam subjected to a static test load, discrete signals were obtained, represented as several harmonic components recorded at all measurement locations. The applied *Imm_DF_system_2021*, used in combination with a reference mechanical device, enabled the registration of displacements at the end of each loading stage. A clear advantage of the proposed system over conventional mechanical instruments was observed. The developed system monitors the behavior of a selected point on the beam by means of a laser sensor.

Previous studies [1–4] have shown that the application of 3D laser scanners for the assessment of serviceability limit states is often impractical due to their high cost, complexity, and time-consuming operation. Therefore, the main motivation of this research was the development of a simple and cost-effective monitoring system. Although based on a different principle, a certain analogy exists, as point displacements are also recorded using a laser-based sensor. The VL6180X sensor successfully fulfilled the objectives of the study and demonstrated satisfactory performance. All recorded displacement signals were processed using the same procedure and subsequently validated against the readings obtained from a mechanical dial gauge. Signal processing was performed using spectral analysis combined with a low-pass Butterworth filter.

As shown in Table 1, a difference of 3.08% was observed between the analytical solution and the finite element method (FEM) results for the midspan displacement, which can be attributed to the spatial discretization of the beam in the numerical model. With respect to load duration, the difference between FEM predictions and raw experimental measurements amounted to 0.68% for short-term loading and 0.58% for long-term loading. The larger discrepancy observed under short-term loading is associated with the loading rate and rheological effects under sustained stress. A higher loading rate corresponds to a higher apparent modulus of elasticity, leading to smaller measured deflections and larger deviations from the FEM results. Conversely, slower loading results in a lower effective modulus of elasticity, larger experimental deflections, and smaller differences relative to the numerical model.

A comparison between the FEM results and the filtered displacement signals yielded differences of 0.04% for short-term loading and 0.28% for long-term loading, which can be attributed to the rheological behavior of wood under prolonged static loading. From the standpoint of time representation in FEM analysis, even short-term experimental loading may be regarded as long-term, and therefore the observed deviation of 0.04% (Table 1) is considered expected and may be adopted as a measure of the system accuracy (resolution 0.01 mm). Finally, it can be concluded that the displacement of a point on the beam evolves over a characteristic time interval that depends on the material properties and the applied loading, in accordance with the rheological behavior of wood.

6 Conclusion

Based on the experimental–theoretical investigation, the proposed *Imm_DF_system_2021* demonstrated high accuracy in capturing changes in beam geometry. Several conclusions and observations can therefore be drawn. In IR-based measurements, the laser intensity recorded by the receiving photodiode depends on the amount of reflected radiation, while the signal reflected from the beam surface is governed by the refractive index of the material. The propagation velocity of the laser beam varies with the medium through which it travels (e.g., air or water), whereas the treated solid material of the beam does not allow transmission. The reflected-signal intensity is further affected by surface color, surface finish, material type, surface temperature, and related factors.

Mathematical and software-based filtering of the displacement signal using a first-order low-pass Butterworth filter proved to be effective. The midspan displacement was evaluated as Δ = 37.88 mm, with a deviation of only 0.04% compared with the numerical result obtained by the finite element method (FEM). The DFT-based analysis revealed only negligible differences in vertical displacement when compared with the results obtained from the FFT analysis of the same signal. Numerical simulations further indicated a pronounced influence of stress on shrinkage and swelling processes, which are characteristic of the mechano-sorptive behavior of wood [28]. Finally, the results indicate that the structural response of the beam depends on both the loading configuration and the natural in-situ moisture variation cycle.

CRediT Authorship contribution statement

Ilija M. Miličić: Conceptualization, Data curation, Funding acquisition, Investigation, Methodology, Resources, Software, Validation Writing - original draft, Writing - review & editing

Radomir J. Folić: Supervision, Visualization, Writing - original draft, Writing - review & editing

Aleksandar D. Prokić: Supervision, Visualization, Writing - original draft, Writing - review & editing

Statements and declarations

Competing Interests The authors declare that they have no known competing financial interests or personal relationships that could have influenced the work reported in this paper.

Ethical Approval and Consent to Participate The work is entirely original and has not been published elsewhere in any form or language.

Consent to Publication All participants give their consent for their work to be published in this journal.

Availability of Data and Materials The datasets generated during the study are available from the corresponding author upon request.

References

[1] LJ.M. Vlajić, I.M. Miličić, M. Romanić, Metodologija skeniranja deformacija na primeru drumskog lančanog mosta (Most preko Tise na putu Kanjiža–Novi Kneževac), Zbornik radova Građevinskog fakulteta 13, Subotica, 2004, str. 206–211

[2] LJ.M. Vlajić, I.M. Miličić, U. Brajković, Novi postupak za registrovanje promene geometrije mostovskih konstrukcija, Zbornik radova Građevinskog fakulteta 15, Subotica, 2006

[3] I.M. Miličić, System for detecting changes in geometry of bridge structures, 10th International conference DQM, June 13–14, Belgrade, Serbia, 2007, p.p. 779–78

[4] I.M. Miličić, LJ.M. Vlajić, R. Folić, U. Brajković, 3D laser scanning deflections on suspension bridge over the river Tisa, 12th International Conference, Structural Faults & Repair – 2008, Edinburgh, Scotland, UK. Edited by: Professor M.C. Forde, PhD, CEng, FREng, FRSE, FICE, FIET. ISBN 0–947644–62–7, 2008, p.p.10

[5] S. Bertuletti, A. Cereatti, D. Comotti, M. Caldara, U.D. Croce, Static and Dynamic Accuracy of an Innovative Miniaturized Wearable Platform for Short Range Distance Measurements for Human Movement Applications, Sensors 2017,17(7),1492, https://doi.org/10.3390/s17071492

[6] VL6180X, Datasheet - production data, ST life, augmented „ Proximity and ambient light sensing (ALS) module, DocID026171 Rev 7, 2016

[7] STMicroelectronics VL6180X Official Web Page. Available online: http://www.st.com/content/st_com/en/products/imaging-and-photonics-solutions/proximity-sensors/vl6180x.html (accessed on 1 May 2017).

[8] STMicroelectronics, VL6180X Proximity and ambient light sensing (ALS) module, Datasheet, Genf, 2016

[9] R. Gunadi, Rosalina, H. Ramza, Alat Ukur Kedalaman Lubang Digital Dengan Memanfaatkan VL6180X (Hole Depth Digital Gauge Using VL6180X), Journal of Electrical Engineering Acta, e-ISSN No.2798-477X, Vol. 1, No.1, 2021, pp. 26-33 DOI:10.22236/ate.v1i1.7215

[10] https://en.wikipedia.org/wiki/Arduino (2024)

[11] The MathWorks, Inc. (2021). MATLAB version 9.10.0.1613233 (R2021a), 2021.

[12] S. Komarizadehasl, B. Mobaraki, H. Ma, J.A. Lozano-Galant, J. Turmo, Low-Cost Sensors Accuracy Study and Enhancement Strategy.*Appl. Sci* 2022, *12*, 3186. https://doi.org/10.3390/app12063186

[13] J. Döring, L. Tharmakularajah, J. Happel, K.L. Krieger, A novel approach for road surface wetness detection with planar capacitive sensors, J. Sens. Sens. Syst. 8, pp. 57-66, https://doi.org/10.5194/jsss-8-57-2019, 21 January 2019.

[14] P. Novotny, N. Ferrie, Using infrared sensor and the Phong illumination model to measure distance, In International Conference on Robotics and Automation, Detroit, Michigan, 1999

[15] L. Korba, S. Elgazzar and T. Welch, "Active Infrared Sensors for Mobile Robots," in IEEE Transactions on Instrumentation and Measurement, 1994

[16] D.P. Baxter, Proximity sensor having an array of single photonavalanche dodes and circuitry for switching off llumination source and assocated method, computer readable medium and firmware, GB/Edinburgh Patent US 8,610,043 B2, 17 12 2013

[17] Ш.Д. Михелев, В.И. Рунов, И.А. Глубцов, Геодезические измерения при изучении деформаций крупных инженерных сооружений, Москва "Недра", 1977. стр. 9-11

[18] I.M. Miličić, M.J. Romanić, Teorijska analiza dinamičkih uticaja 1D modela pobuđenog dejstvom spoljašnjih pomeranja, Savremena dostignuća u građevinarstvu (3; Subotica;2015), ISBN 978-86-80297-62-0, str. 341-350

[19] I.M. Miličić, A. Prokić, R. Folić, Matematičko modeliranje odziva 1D modela sa otporom podloge primenom Furijeve transformacije, Međunarodno naučno-stručno savetovanje Zemljotresno inženjerstvo i inženjerska seizmologija (5; Sremski Karlovci; 2016), ISBN 978-86-88897-08-2, str. 273-282

[20] I.M. Miličić, A. Prokić, Đ. Lađinović, Computer simulation of the order frequencies amplitudes excitation on response dynamic 1D models, Conference proceedings 5th international conference contemporary achievements in civil engineering, 2017, DOI:10.14415/konferencijaGFS2017.032, ISBN 978-86-80297-68-2, pp. 311-320

[21] I.M. Miličić, Đ. Lađinović, I.I. Miličić, Computer simulation 1D model excited of two frequent by the action of external displacement – part 1, Conference proceedings 6th international conference contemporary achievements in civil engineering, 2018, DOI:10.14415/konferencijaGFS2018.016, ISBN 978-86-80297-73-6, pp.183-192

[22] I.M. Miličić, A. Prokić, R. Folić, Computer simulation 1D model excited of two frequent by the action of external displacement – part 2, Conference proceedings 6th international conference contemporary achievements in civil engineering 2018,

DOI:10.14415/konferencijaGFS2018.017, ISBN 978-86-80297-73-6, pp. 193-202
[23] I.M. Miličić, M. Kekanović, V. Aladžić, I.I. Miličić, Harmonic analysis there frequency response with views of the number of members of the series „FFT“ transformation, Journal of faculty of civil engineering 36 (2019), UDK:004.942:531.3 DOI: 10.14415/zbornikGFS36.02
[24] S. Butterworth, On the Theory of Filter Amplifiers, Experimental Wireless and the Wireless Engineer. 7, 1930, pp. 536–541
[25] L.P. Huelsman, An equal-valued capacitor active RC network realization of a fourth-order low-pass Butterworth characteristic, Proceedings of the IEEE. 62 (12): 1709. December 1974, doi:10.1109/PROC.1974.9689
[26] G. Bosse, Siebketten ohne Dämpfungsschwankungen im Durchlaßbereich (Potenzketten), Frequenz. 5(10): 279–284. Bibcode:1951Freq. 5. 279B. 1951, doi:10.1515/FREQ.1951.5.10.279. S2CID 124123311
[27] G. Bianchi, R. Sorrentino, Electronic filter simulation & design. McGraw-Hill Professional. pp.17–20.2007, ISBN978-0-07-149467-0
[28] J. Strömbro, P. Gudmundson, Mechano-sorptive creep under compressive loading – A micromechanical model, International Journal of Solids and Structures, Volume 45, Issue 9, 2008, pp 2420-2450